Nanoscale

PAPER

View Article Online
View Journal | View Issue



Cite this: *Nanoscale*, 2026, **18**, 3723

# A synergistic ZnO/FAPbBr$_3$ nanocrystal n–n heterojunction for low-bias, fast, broadband photodetection and memristive applications

Monisha Nayak,[a] Ashutosh Mohanty,[b] Pragalbh Kashyap,[c] Abhijit Bar[d] and Sudip K. Saha *[a]

Heterojunctions formed between metal halide perovskites and wide-bandgap oxides have emerged as a powerful platform for broadband photodetection, leveraging their complementary optoelectronic properties and tunable interfacial dynamics. In this study, we demonstrate the synergistic integration of an n–n type-II ZnO/FAPbBr$_3$ nanocrystal (NC) heterojunction, enabling efficient broadband photodetection at low bias voltages with rapid response characteristics. Under white light illumination (48.27 mW cm$^{-2}$), the device achieves peak photoresponse at a 1 V bias, exhibiting an impressive on/off current ratio of ~1.44 × 10$^4$, a responsivity of 0.668 A W$^{-1}$, and a specific detectivity of 7.78 × 10$^{11}$ Jones. The engineered interface facilitates effective charge separation and transport, while the spectral overlap between ZnO and FAPbBr$_3$ NCs extends the photoresponse across the visible and near-UV regions. Notably, the device demonstrates a fast temporal response with rise and fall times of 80 μs and 90 μs, respectively—making it suitable for high-speed imaging applications. Additionally, cyclic voltage sweeps reveal an analog switching behavior, indicative of gradual conductance modulation. This memristive-like response suggests potential utility in neuromorphic systems, where such analog switching can emulate synaptic functionalities. Overall, the ZnO/FAPbBr$_3$ NC heterojunction exemplifies a multifunctional architecture, combining high-performance photodetection with prospects for artificial synapse implementation in next-generation neuromorphic electronics.

Received 14th October 2025,
Accepted 16th December 2025

DOI: 10.1039/d5nr04337a

rsc.li/nanoscale



## 1. Introduction

In the realm of modern science and technology, efficient and reliable optical detection systems serve as a foundational pillar, propelling advancements in high-resolution imaging, environmental monitoring, optical communication, industrial automation, and biomedical sensing.[1–5] At the heart of these systems lies the photodetector—an electronic device that simultaneously detects and converts incident photon flux into electrical signals. Conventional photodetectors based on inorganic semiconductors such as silicon (Si), gallium nitride (GaN), and indium gallium arsenide (InGaAs) offer notable advantages, including band-selective detection, high sensitivity, thermal stability, low noise, and rapid response times.[6–14] However, their reliance on expensive growth techniques, complex fabrication processes, high operating voltages, and limited transparency and flexibility poses significant challenges.[15] This has spurred the search for alternative semiconducting materials that combine excellent optical properties with simpler, cost-effective processing.

Metal halide perovskites (MHPs) have emerged as promising candidates due to their tunable direct bandgap, high absorption coefficients across the UV–Vis–NIR spectrum, long carrier diffusion lengths, and high mobilities.[16] Moreover, their compatibility with low-temperature, solution-based fabrication methods offers a distinct advantage over traditional semiconductor technologies.[17,18] A landmark study by Dou *et al.* in 2014 demonstrated the first hybrid perovskite photodetector based on MAPbI$_{3-x}$Cl$_x$, achieving a detectivity of 10$^{14}$ Jones—comparable to state-of-the-art inorganic devices.[19]

Structurally, metal halide perovskites (MHPs) adopt the general formula ABX$_3$, where A, B and X represent distinct ionic sites. The A-site accommodates either an organic cation (*e.g.*, formamidinium and methylammonium) or an inorganic cation (*e.g.*, cesium), while the B-site hosts a metal cation such

[a]*Department of Physics, Diamond Harbour Women's University, Sarisha, South 24 Parganas, West Bengal 743368, India. E-mail: sudipsahaju@gmail.com*
[b]*Department of Physics, School of Advanced Science (SAS), Vellore Institute of Technology (VIT), Vellore 632014, Tamil Nadu, India*
[c]*Department of Physics, Indian Institute of Technology Guwahati, Assam 781039, India*
[d]*Department of Physics, Jogesh Chandra Chaudhuri College, West Bengal, 700033, India*

as lead (Pb) or tin (Sn). The X-site is occupied by halide anions —iodide ($I^-$), bromide ($Br^-$), or chloride ($Cl^-$). The formation and stability of these compounds are governed by their octahedral geometry and tolerance factor criteria.[20] The slightly larger formamidinium cation ($FA^+$) tends to yield compounds with greater thermal stability compared to methylammonium ($MA^+$). Moreover, $FAPbX_3$ (where X = $I^-$ and $Br^-$) perovskites exhibit optimal bandgaps, making them well suited for energy-harvesting applications.[21–27] Recent advancements in FA-based photodetectors have focused on $FAPbI_3$ and $FAPbBr_3$ compounds across diverse morphologies—including single crystals,[28] polycrystalline films,[29] quantum dots,[30] two-dimensional structures,[31] and one-dimensional arrays[32,33]—revealing a range of compelling optoelectronic properties. Reports suggest that $FAPbX_3$, in conjunction with other suitable conducting or semiconducting materials such as graphene,[34] germanium,[35] and nickel oxide,[36] can enhance the charge transfer properties at the interface due to the inherent built-in field.

The integration of wide-bandgap metal oxides with light-absorbing materials has emerged as a powerful approach to enhance photodetector performance by balancing sensitivity and speed. In particular, metal oxide/perovskite heterostructures are highly effective, as the oxide layer contributes high electron mobility, environmental stability, and defect passivation to the photoactive perovskite. Among various candidates, zinc oxide (ZnO) is often favored over alternatives such as $TiO_2$ due to its superior electron transport properties and compatibility with low-temperature processing, which together enable ultrafast device response.[37–40] In parallel, ZnO-based heterojunctions with various perovskites ($MAPbI_3$, $CsPbBr_3$, $Cs_2SnI_6$, $Cs_3Bi_2I_9$, *etc.*) achieved higher detectivities and response times down to microseconds, underscoring ZnO's role as a robust electron transport layer.[41–52]

In essence, the combination of a high-quality photosensitive material with a well-conceived architectural design strategy can lead to highly efficient photodetectors exhibiting remarkable figures of merit. From a structural standpoint, photodetectors are broadly categorized into photoconductors, phototransistors, and photodiodes—each offering distinct operational mechanisms and performance characteristics.[53,54] Photoconductors possess a metal–semiconductor–metal architecture with a vertical or lateral arrangement and an internal gain mechanism due to the recirculation of a single type of charge carrier across the electrodes. Phototransistors are three-terminal (source, drain, and gate) lateral structures with additional biasing at the gate terminal to control the carrier dynamics and photocurrent gain of the device. A photodiode is essentially a vertical arrangement in which the photosensitive material is sandwiched between two charge-separating layers. Under the influence of a built-in field and/or a reverse-bias voltage, the carriers drift towards the respective electrodes. Given the advantages of simple fabrication steps and faster response times due to closer electrodes, photodiodes are often preferred over the other two configurations. The built-in electric field in a photodiode is primarily achieved using a p–i–n junction, a p–n junction, or a Schottky junction. Although photodiodes comprising an isotype heterojunction (n–n/p–p) are less frequently observed, they have been reported to offer significant benefits in terms of device performance. For instance, a type-II heterojunction formed between two different n-type materials creates a depletion region and an accumulation region depending on the Fermi-level alignment of the materials.[55] A built-in field is thus generated across the junction, aiding the movement of majority carriers to produce a photoresponse. Because only the majority charge carriers are involved, this type of heterojunction can also reduce recombination losses in the device, resulting in a faster response.[55,56] This strategy holds substantial potential but remains comparatively underinvestigated within the landscape of perovskite photodiode architectures, thus opening doors for exploring the impact of n–n heterojunctions with different materials and designs to build photodetectors with faster responses and better performance.

In this study, we investigate the optoelectronic performance of an n–n heterojunction photodetector comprising ZnO and $FAPbBr_3$ nanocrystals (NCs). The device demonstrates broadband capabilities with a pronounced photoresponse under low bias conditions, accompanied by a fast response. Furthermore, it maintains operational stability over a continuous 1-hour period at an applied bias of 0.25 V under white light illumination with an intensity of 80.26 mW $cm^{-2}$ under ambient conditions. The performance parameters of this novel n–n heterojunction architecture are comparable to those of previously reported $FAPbBr_3$-based photodetectors. Notably, the simple vertical configuration (FTO/ZnO/$FAPbBr_3$/Ag) exhibits analog switching characteristics, indicating potential for neuromorphic applications. These findings underscore the multifunctional nature of the device under appropriate biasing conditions. The synergy of speed and sensitivity in the detector underscores its potential for imaging applications in diverse fields, including diagnostics and environmental assessment.

## 2. Experimental methods

### 2.1. Materials

Lead bromide ($PbBr_2$) (≥98%), *N*,*N*-dimethylformamide (anhydrous, 99.8%), oleic acid (≥99%), oleylamine (technical grade, 70%), and zinc oxide dispersion (<10 nm particle size, 20 wt% in $H_2O$) were purchased from Sigma-Aldrich. Formamidinium bromide (99.99%, trace metal basis) was purchased from TCI Chemicals. Toluene (≥99.5%), butanol (anhydrous, 99.8%), ethanol (≥99.9%), acetone (≥99%), hydrochloric acid (30%), and zinc powder were purchased from Merck. All the chemicals were used without any further purification.

### 2.2. Synthesis of $FAPbBr_3$ nanocrystals

The synthesis of $FAPbBr_3$ NCs were carried out using a solution-based emulsion method. A 0.1 mM perovskite precursor was first prepared by taking 0.1 mmol of FABr and 0.1 mmol of $PbBr_2$ properly dissolved in 1 ml of DMF at 60 °C until a transparent solution was obtained. In another vial, a mixture

 

of toluene (5 ml), oleic acid (0.5 ml), oleylamine (0.02 ml) and butanol (1.5 ml) was prepared and rigorously stirred for 5 min at 55–60 °C. The formation of $FAPbBr_3$ NCs was initiated by adding 0.2 ml of the precursor to the antisolvent mixture in a dropwise manner while continuously stirring the mixture at 1100 rpm. The colourless mixture soon transformed into a luminescent yellowish solution, indicating the formation of nanoparticles, and the mixture was immediately removed from the heating and stirring conditions to limit the formation of larger particles. After allowing the solution to cool naturally for 5 min, the purification of NCs was carried out to wash off the excess ligands and unwanted larger particles from the NC solution in two steps. In the first step, the crude solution was centrifuged at 5500 rpm for 8 min. The precipitate was redispersed in a mixture of toluene and ethyl acetate to ensure the removal of excess ligands from the surface of the NCs. Finally, the precipitate obtained thereafter was redispersed in toluene as per further requirements for characterization and device fabrication. The entire process of synthesis and purification was carried out under ambient conditions with relative humidity between 50% and 80%.

### 2.3. Device fabrication

FTO substrates were etched using zinc powder and hydrochloric acid, and later washed with soap solution, distilled water, acetone, and ethanol using a standard procedure for 15 min each. The etched and dried substrates were subjected to UV-ozone treatment for another 15 min before use. Firstly, a ZnO layer was spin-coated using the commercially available dispersion at 3000 rpm for 30 s and then annealed at 100 °C for 30 min. Furthermore, a toluene-dispersed NC solution of $FAPbBr_3$ was used to form the perovskite layer. To achieve the desired thickness for this layer, the NC dispersion was spin-coated several times at 1600 rpm for 30 s each and finally annealed at 60–70 °C for 15 min. To complete the device architecture, a 70 nm thick layer of Ag was thermally evaporated over the perovskite layer at a pressure of $10^{-6}$ mbar. All the spin-coating and annealing procedures were carried out under ambient conditions with 50–80%RH.

## 3. Material and device characterization

The crystallinity and phase identification of the prepared perovskite samples were determined from X-ray diffraction (XRD) patterns using a Bruker D2 Phaser with a Cu-Kα radiation source of 1.5406 Å wavelength. The morphological features of the perovskite thin film were investigated using Field Emission Scanning Electron Microscopy (FESEM) with a Gemini 500 FE-SEM. The shape and size of the perovskite nanocrystals were analyzed using a High Resolution Transmission Electron Microscope (HR-TEM) (FEI Tecnai, Model: G2-20 TWIN) at an operating voltage of 200 kV. To investigate the chemical composition of the perovskite samples, we opted for X-ray Photoelectron Spectroscopy (XPS) using an ULVAC-PHI (Model: VersaProbe 4). The SEM cross-sectional analysis was done using a Thermo Fisher Scientific FEI Quanta 250 FEG. The optical UV-Vis absorption spectra of the $FAPbBr_3$ NCs were obtained using a Cary 60 UV-Vis Spectrophotometer. Photoluminescence spectra of the perovskite samples with an excitation wavelength of 450 nm were recorded using a Cary Eclipse Fluorescence Spectrophotometer. The transient-state PL of the perovskite samples was further elucidated using a Fluorolog time-correlated single-photon counting spectrometer (Horiba Scientific) with a delta diode laser. The energy band levels of the $FAPbBr_3$ samples were determined from ultraviolet photoelectron spectroscopy using a Thermo Scientific NEXSA system. The spectral response of the device was measured with the help of a spectral response measurement apparatus (Holmarc, Model: HO-AE-SR18). All the *I–V* measurements were carried out using a Keithley 2461 source meter. A portable solar simulator (PEC-L01) was used as the source of white-light illumination for the photodetection measurements. The transient measurements were carried out with the help of an oscilloscope (Teledyne LeCroy WaveSurfer 3000Z series oscilloscope), a function generator (Tektronix AFG 3022C) and a green LED (530 nm) with variable power.

## 4. Results and discussion

$FAPbBr_3$ NCs were synthesized *via* a low-temperature emulsion-based methodology. The X-ray diffraction (XRD) pattern of the resulting thin film (Fig. 1a) confirms a cubic crystal phase, with prominent peaks at 14.6°, 29.6°, and 45.3°, corresponding to the (001), (002), and (003) crystallographic planes, respectively. Additional peaks at 20.8°, 33.3°,36.48° and 42.5° are attributed to the (011), (021), (211) and (022) planes, in good agreement with previously reported data.[57] The average particle size of the NCs was estimated to be 29.44 nm using the Debye–Scherrer equation ($D = K\lambda/B\cos\theta$), with a calculated lattice parameter $a$ = 4.82 Å. Transmission electron microscopy (TEM) analysis (Fig. 1b) reveals predominantly cubic-shaped NCs, albeit with some degree of polydispersity. The corresponding histogram (Fig. 1c) indicates a size distribution of 10.52 ± 1.27 nm. Selected area electron diffraction (SAED) patterns (Fig. 1d) further confirm the polycrystalline nature of the NCs, with diffraction spots aligning well with the XRD reflections, reinforcing the cubic phase assignment. Scanning electron microscopy (SEM) images of $FAPbBr_3$ NCs deposited on glass substrates (Fig. 1e) show a slightly inhomogeneous surface morphology, characterized by minimal pinholes and adequate film coverage. Additionally, we analysed the cross-sectional SEM of the device shown in Fig. S1.

To elucidate the elemental composition and chemical states of the synthesized $FAPbBr_3$ NCs, X-ray photoelectron spectroscopy (XPS) analysis was performed. The survey spectrum (Fig. 2a) confirms the presence of all expected constituent elements—carbon (C), nitrogen (N), lead (Pb), and bromine (Br)—alongside oxygen (O), with no evidence of extraneous peaks.[58] High-resolution spectra reveal distinct Pb

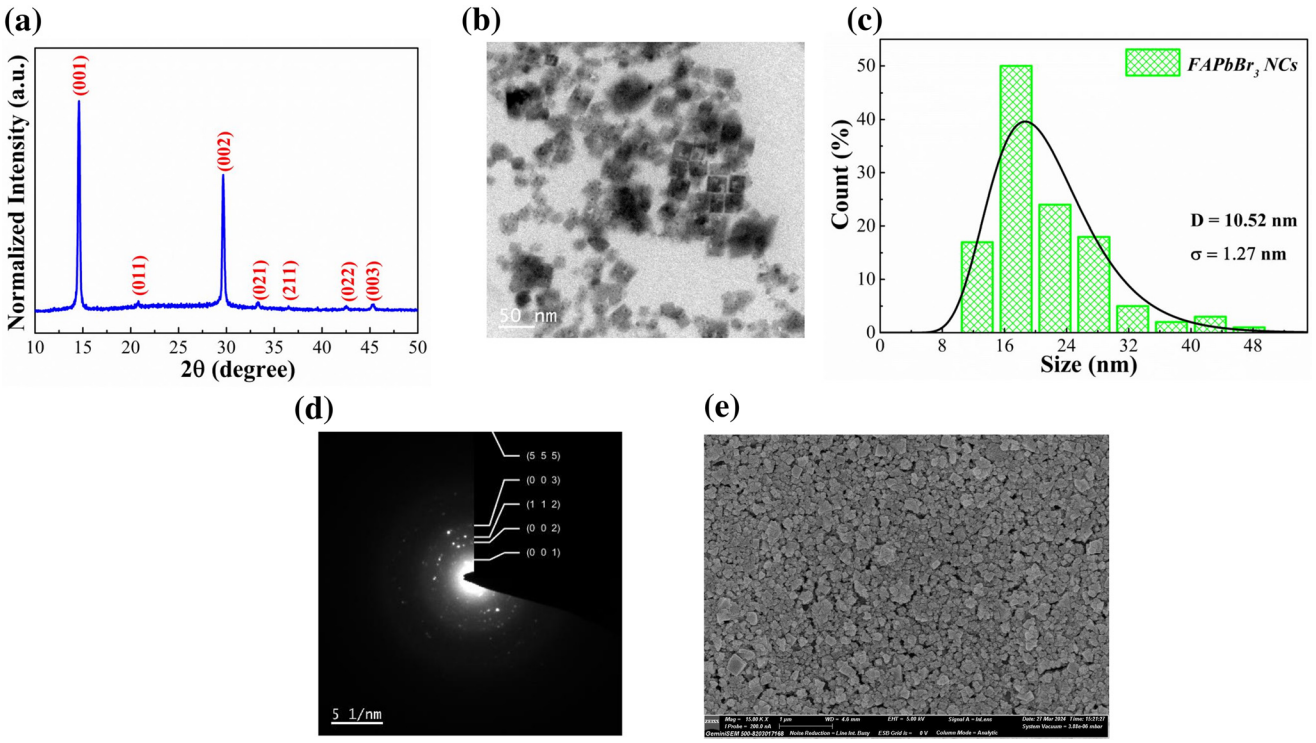


Fig. 1 (a) X-ray diffraction pattern. (b) TEM images depicting particles at the 100 nm scale. (c) Histogram depicting the size distribution for $FAPbBr_3$ NCs. (d) SAED pattern. (e) FESEM image for $FAPbBr_3$ NCs.

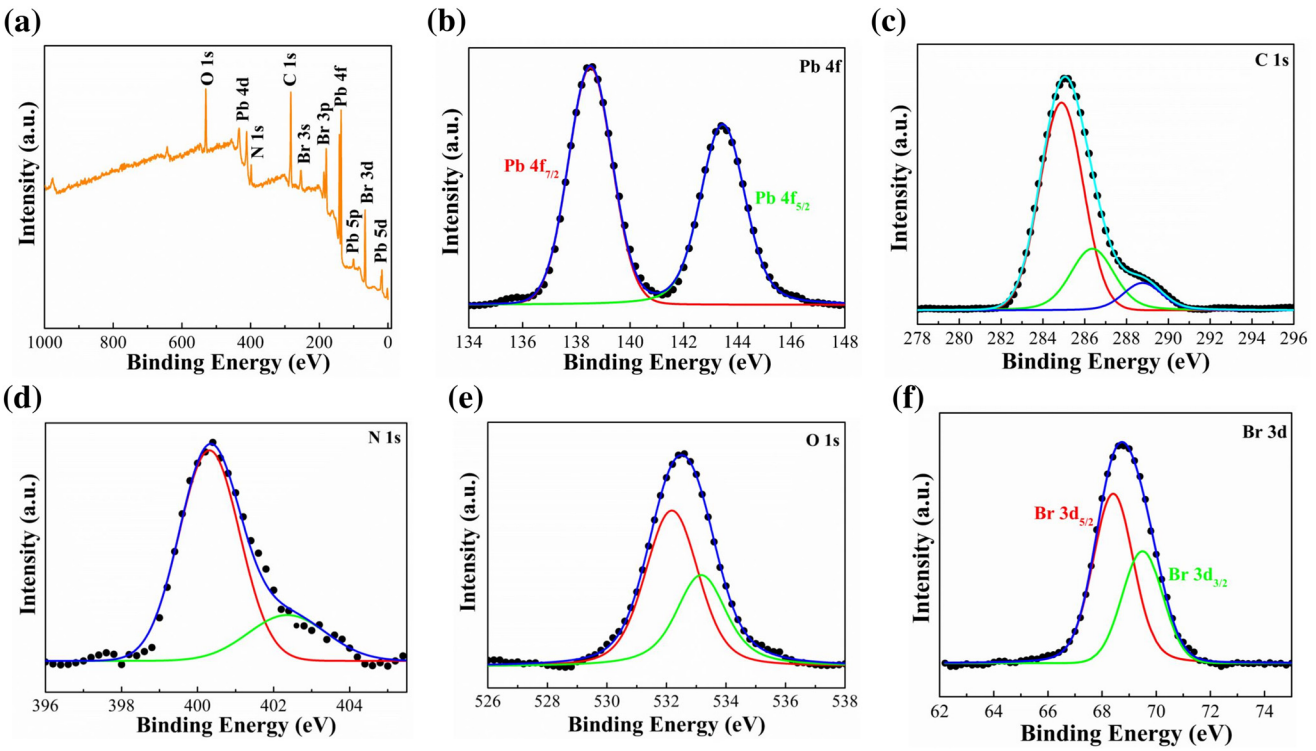


Fig. 2 XPS for $FAPbBr_3$ showing (a) Survey spectra and high-resolution spectra for (b) Pb 4f, (c) C 1s, (d) N 1s, (e) O 1s and (f) Br 3d.

4f doublets at approximately 138.5 eV and 143.4 eV, corresponding to the spin–orbit split components of Pb $4f_{7/2}$ and Pb $4f_{5/2}$, respectively. The Br 3d region exhibits deconvoluted peaks at ~68.6 eV and ~69.2 eV, confirming the presence of bromine in the perovskite lattice. Similarly, the N 1s spectrum shows peaks at ~400.3 eV and ~402.3 eV, indicative of nitrogen bonding environments associated with formamidinium and amine-based surfactants. The C 1s spectrum reveals three distinct peaks centered at 284.8 eV, 286.3 eV, and 288.7 eV, corresponding to C–C, C–H, C–N, and C═O bonding configurations, respectively. Additionally, the O 1s region displays two deconvoluted peaks at 532.1 eV and 533.1 eV, attributed to carboxylic functionalities, with the higher-energy peak (533.1 eV) arising from O–C═O bonds.

To determine the optical characteristics of $FAPbBr_3$ NCs, we investigated their UV–Visible absorption, steady-state, and time-resolved photoluminescence spectra. As illustrated in Fig. 3a, the NCs exhibit a pronounced photoluminescence peak at 540 nm, accompanied by good absorption across the visible spectrum. The corresponding optical bandgap is estimated to be approximately 2.2 eV from the Tauc plot (Fig. 3b), aligning well with reported values.[58,59] Additionally, the transient PL study of the NC sample (Fig. 3c) at a laser excitation of 350 nm indicates a slow tri-exponential decay, with an average carrier lifetime of 67 ns.[58]

Using the Ultraviolet Photoelectron Spectroscopy (UPS) technique, we further estimated the Fermi energy ($E_F$), valence band maximum ($E_{VBM}$), and conduction band minimum ($E_{CBM}$) of the $FAPbBr_3$ NCs. The secondary electron cut-off edge and the valence band cut-off region are depicted in Fig. 3d and e. The $E_F$ is determined by subtracting the cut-off edge of the secondary electrons, *i.e.*, 16.04 eV, from the energy of the incoming HeI electrons (21.22 eV), giving the following value:

$$16.1\ \text{eV} - 21.22\ \text{eV} = -5.12\ \text{eV} = E_F \quad (1)$$

From Fig. 3e, the onset of the valence band edge is found to be at 1.16 eV, which reflects the difference between $E_{VBM}$ and $E_F$. Using this information, we calculated $E_{VBM}$ as −6.28 eV and hence, $E_{CBM}$ is found to be −4.08 eV from the following relation:

$$E_{CBM} = E_g + E_{VBM} \quad (2)$$

Therefore, $E_F$, $E_{VBM}$ and $E_{CBM}$ are positioned at −5.12 eV, −6.28 eV and −4.08 eV, respectively, and from the Fermi level position, an n-type character for $FAPbBr_3$ NCs.

The following section discusses the role of the ZnO/$FAPbBr_3$ heterojunction and its subsequent device performance as a broadband photodetector and potential memory device.

**I. The n–n ZnO/$FAPbBr_3$ heterojunction as a photodetector:**

Here, we designed a visible-range, broadband photodetector with a simple vertical architecture, FTO/ZnO/$FAPbBr_3$/Ag, that incorporates a ZnO/$FAPbBr_3$ NC n–n heterojunction. FTO and Ag, respectively, serve as the bottom and top electrodes, allow-

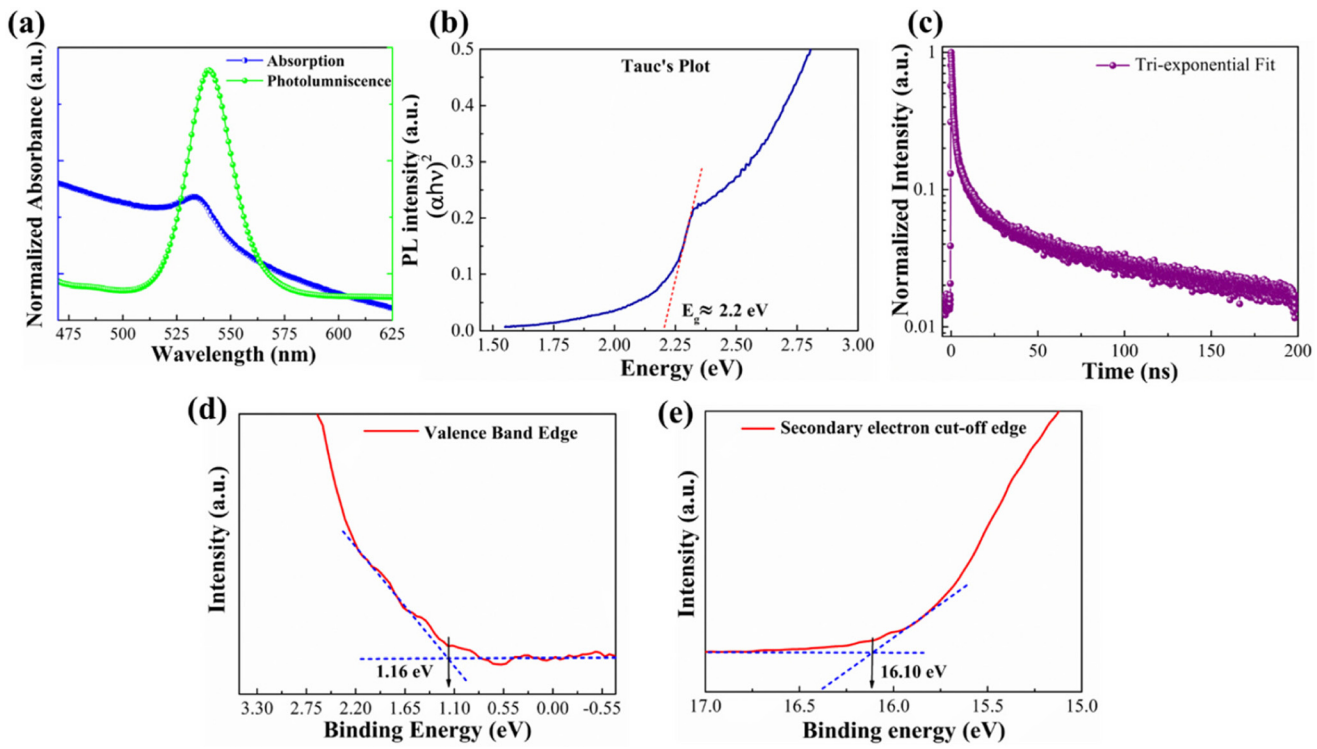


**Fig. 3** (a) UV-Vis absorption and PL study for $FAPbBr_3$ thin films. (b) Tauc plot. (c) Transient PL study for toluene dispersed samples. UPS for $FAPbBr_3$ NCs estimating (d) the work function from the onset of photoemission spectra and (e) valence band maximum onset.

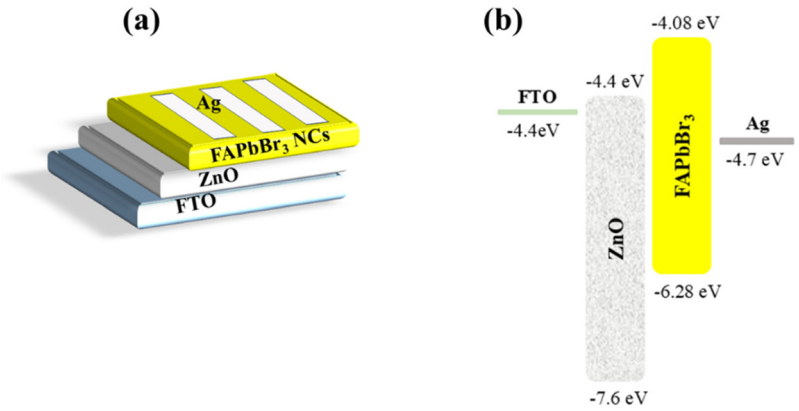


**Fig. 4** (a) Device arrangement of the photodiode-type photodetector with the ZnO/$FAPbBr_3$ NC heterojunction, Ag and FTO functioning as the top and bottom electrodes, respectively. (b) Energy-band diagram of the photodetector.

ing for electrical connections. The spectral response of the device shows a broad absorption range, as presented in Fig. S2. The device arrangement and the concerned band alignment among the layers are depicted in Fig. 4a and b. We achieved the targeted broad range of detection by applying a white light source. Fig. 5a shows the semi-logarithmic *I–V* curve of the ZnO/$FAPbBr_3$ heterojunction for the voltage range of ±2 V, under dark and white light illumination. As evidenced, the device shows rectifying *I–V* characteristics along with a significant rise in current levels under illumination. This confirms the good photodetection ability of our n–n heterojunction device under irradiation. For a more detailed analysis, the photoresponse behavior of the device was investigated under a constant reverse bias using a Keithley source meter. The measurements were conducted over a defined time interval with manually controlled cyclic transitions between dark (off) and illuminated (on) conditions to evaluate the device's responsiveness and stability. Fig. 5b shows the corresponding *I–t* curve of the device at a reverse bias voltage of 0.25 V under an incident light intensity of 80.26 mW $cm^{-2}$, where the photocurrent shoots and then falls back respectively at each light "on" and "off" interval of 10 seconds each. The sharp edges at the rise and fall intervals predict the fast performance of our detector. Additionally, the ratio of the photocurrent at one of such intervals, that is the on/off ratio ($I_{on/off}$), is approximately $3 \times 10^3$, signifying good performance.

Furthermore, the operational stability of the device was tested for an extended period of 1 h under the same conditions of bias voltage, illumination, and on–off interval. As depicted in Fig. 6a, the device showed a good repeatability over an increased number of cycles, confirming stable photodetection. A zoomed-in image of Fig. 6a shows the first and last 15 min performance of the photodetector with almost no degradation in photodetection over the period, as presented in Fig. 6b and c, respectively. This preliminary characterization suggests that the ZnO/$FAPbBr_3$ heterojunction device is capable of generat-

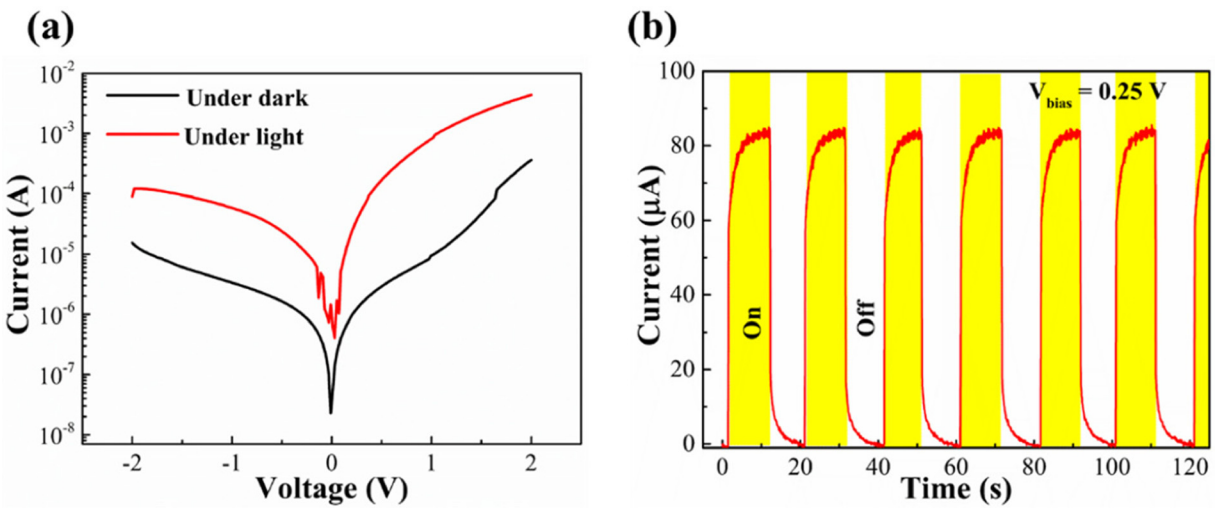


**Fig. 5** (a) Semi-logarithmic *I–V* characteristics for FTO/ZnO/$FAPbBr_3$/Ag. (b) *I–t* curve depicting the photoresponse behavior of the device under 80.26 mW $cm^{-2}$ at a reverse bias voltage of 0.25 V for a 10 s on–off interval.

 

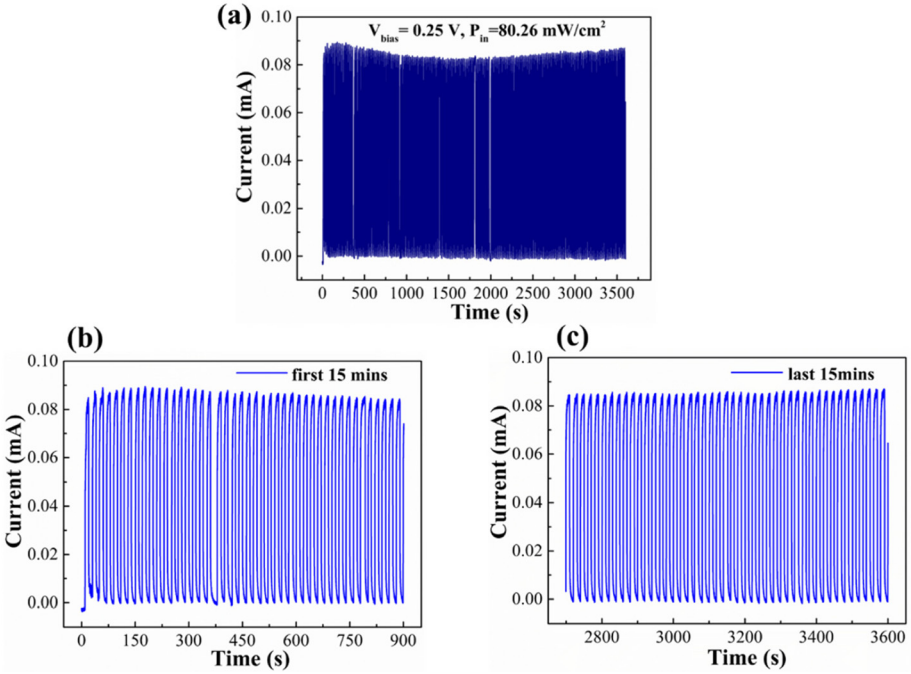


**Fig. 6** (a) Operational stability tested for 1 h with multiple switching cycles. The enlarged view for the (b) first 15 min and (c) last 15 min of the testing period.

ing an almost instantaneous photoresponse to detect incident light at a relatively low bias. To further characterize our device, we outline three important figure-of-merits for a photodetector: responsivity, specific detectivity, and response speed.

The responsivity ($R$) of a photodetector determines the efficiency of conversion of an incoming light signal to an electrical signal and is determined using the following expression:

$$R = J_{ph}/P_{inc} \quad (3)$$

where

$$J_{ph} = I_{ph}/A = (I_{light} - I_{dark})/A \quad (4)$$

$R$ is often expressed in units of A W$^{-1}$ or mA W$^{-1}$.

The second important parameter is specific detectivity ($D^*$), which estimates the ability of a photodetector to detect the weakest of the incoming light signals and is given as:

$$D* = A^{1/2}R/(2qI_{dark}) \quad (5)$$

$D^*$ is often expressed in units of Jones.

The third important parameter is the response speed of the photodetector, which measures how fast a change in the output signal is achieved based on detectable changes in the incoming photon flux. Notably, for a detector, we specify the rise time ($\tau_r$) and fall time ($\tau_d$) based on the time required for the photocurrent to change from 10% to 90% of the maximum output signal and *vice versa*, respectively. For an active device area of 4 mm$^2$, the $R$ and $D^*$ at 0.25 eV biasing under an irradiance of 80.26 mW cm$^{-2}$ (Fig. 5b) were calculated to be 26.43 mA W$^{-1}$ and 6.16 × 10$^{11}$ Jones, respectively. The effect of bias voltages and incident light intensities on the device performance was examined through various sets of measurements. Fig. 7a depicts the $I$–$t$ curves corresponding to various applied voltages at a constant irradiance of 58 mW cm$^{-2}$. The photoresponse of the detector was found to rise with increasing bias, implying a better collection of photogenerated carriers under a stronger electric field. As shown in Fig. 7b, the subsequent values of $R$ and $D^*$ also outline a rising trend, with their respective highest values 79.4 mA W$^{-1}$ and 0.99 × 10$^{10}$ Jones at 0.9 V bias voltage.

In another set of measurements, we recorded the $I$–$t$ curves at a fixed bias voltage of 0.5 V over different values of incident light intensities ranging from 40.19 mW cm$^{-2}$ to 137.32 mW cm$^{-2}$, as depicted in Fig. 7c. Fig. 7d presents the $R$ and $D^*$ values at different light intensities extracted from Fig. 7c. The maximum values of $R$ and $D^*$ were calculated to be 63.8 mA W$^{-1}$ and 0.95 × 10$^{10}$ Jones, respectively, at a light intensity of 40.19 mW cm$^{-2}$ and a bias voltage of 0.5 V. Notably, the parameters $R$ and $D^*$ exhibit a diminishing trend at higher light intensities. This behaviour is commonly attributed to enhanced scattering and recombination of charge carriers, resulting from elevated photogeneration rates at higher incident power densities.[35,52,60] Here, the photocurrent exhibits a modest increase with higher light intensities. Using linear curve fitting, we can estimate the power-law dependence of the photodetector using the following equation:

$$I_{ph} \propto P^m \quad (6)$$

where $I_{ph}$ stands for the photocurrent, $P$ is the incident optical power and $m$ is the exponent reflecting the ratio of generation

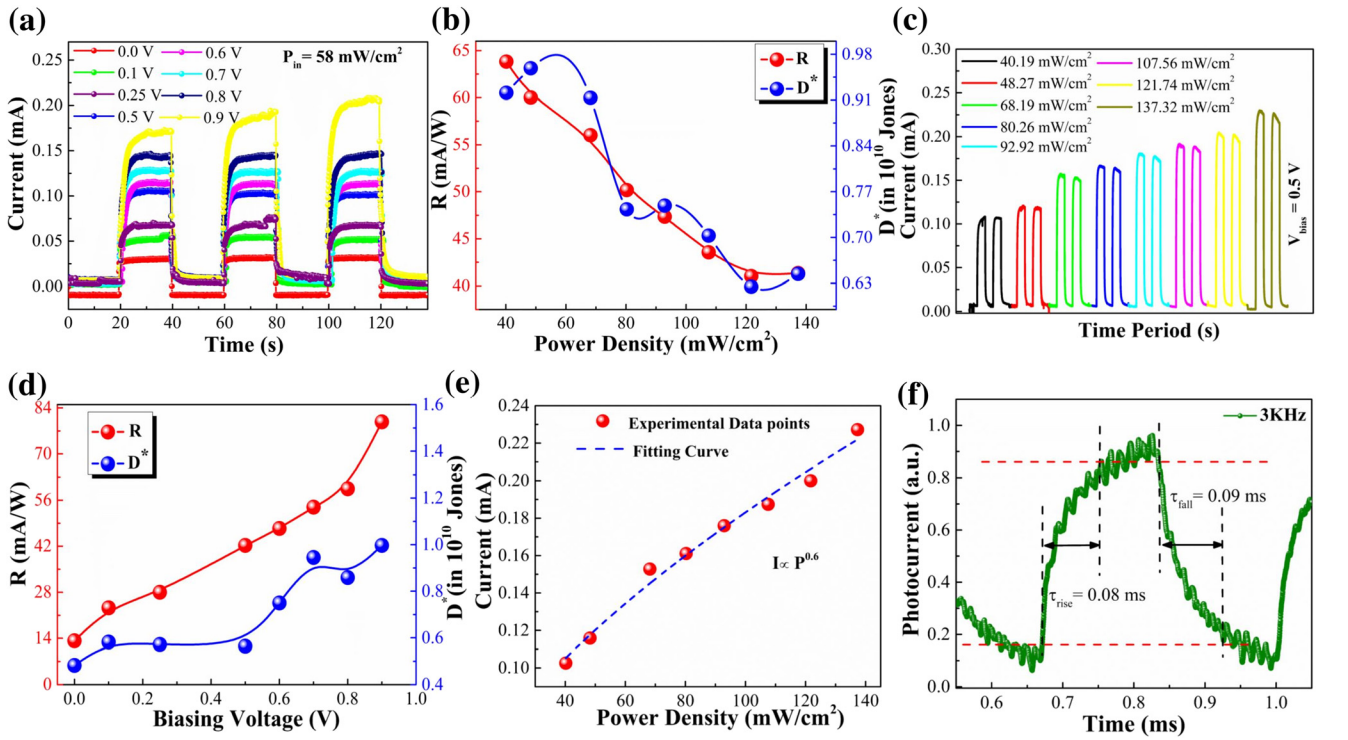


**Fig. 7** (a) Time-dependent photocurrent under different bias voltages for FTO/ZnO/FAPbBr$_3$/Ag. (b) Responsivity and specific detectivity as a function of bias voltages at 58 mW cm$^{-2}$ white light intensity. (c) Intensity-dependent behavior of the FTO/ZnO/FAPbBr$_3$/Ag device at 0.5 V reverse biasing under various white light intensities. (d) Responsivity and specific detectivity as a function of different light intensities at 0.5 V bias voltage. (e) Power-law dependence of the photocurrent, (f) rise ($\tau_{rise}$) and fall ($\tau_{fall}$) time of the device under 530 nm illumination at 3 kHz transient frequency.

of carriers to the incident photons. A sublinear relationship with $m$ = 0.6, as shown in Fig. 7e, for our device suggests the presence of trap states or defects in the light-absorbing material or the device. Thus, the above measurements indicate that the ZnO/FAPbBr$_3$ heterojunction photodetector exhibits optimal light detection under low to moderate light intensities when operated with an appropriate reverse bias.

Beyond the capability to detect and transduce optical signals into electrical outputs, the temporal response of a photodetector is a critical parameter that governs its suitability for specific applications. For instance, ultrafast photodetectors with response times on the order of nanoseconds are often employed in optical communication systems to transmit data at high speeds. whereas applications such as image sensing or industrial monitoring can allow longer response times, typically in the microsecond range. To probe the response speed of our detector, we examined the transient response of the device using an oscilloscope-controlled LED (530 nm) setup at various operating frequencies. Fig. 7f shows the normalized photoresponse at 3 kHz frequency with the estimated rise and fall times of 0.08 ms and 0.09 ms respectively. Table 1 lists the rise and fall times for a range of operating frequencies from 100 Hz to 3 kHz. As witnessed, the device shows a lower response time with increasing transient frequency, indicative of a fast-switching behavior with nearby values of rise and fall times.

**Table 1** Rise and fall times of FTO/ZnO/FAPbBr$_3$/Ag at different operating frequencies

| Frequency (kHz) | Rise time (ms) | Fall time (ms) |
|---|---|---|
| 0.01 | 2.28 | 2.32 |
| 0.05 | 0.57 | 0.52 |
| 1.00 | 0.28 | 0.23 |
| 1.50 | 0.17 | 0.21 |
| 2.00 | 0.15 | 0.13 |
| 2.50 | 0.11 | 0.10 |
| 3.00 | 0.08 | 0.09 |

Our device has also been tested under different low intensity light signals of 455 nm (blue) and 530 nm (green) using LED sources. Fig. 8a and b show the *I*–*t* curves for 5 varying LED intensities at a low bias voltage of 0.01 V. A stable response with sharp rise and fall times is observed, signifying the detection of low-intensity light signals. Similar data were recorded at different bias voltages of 0, 0.05, 0.1 and 0.05 V for both 455 nm and 530 nm wavelengths with the corresponding *I*–*t* curves presented in Fig. S3 and S4, respectively.

The photodetector measurements undertaken so far for the ZnO/FAPbBr$_3$ heterojunction structure highlight the efficient functioning of the device over a broad range of detection wavelengths, with low operating voltage and fast switching speed. The sensitivity of the detector to both low and high incoming

 

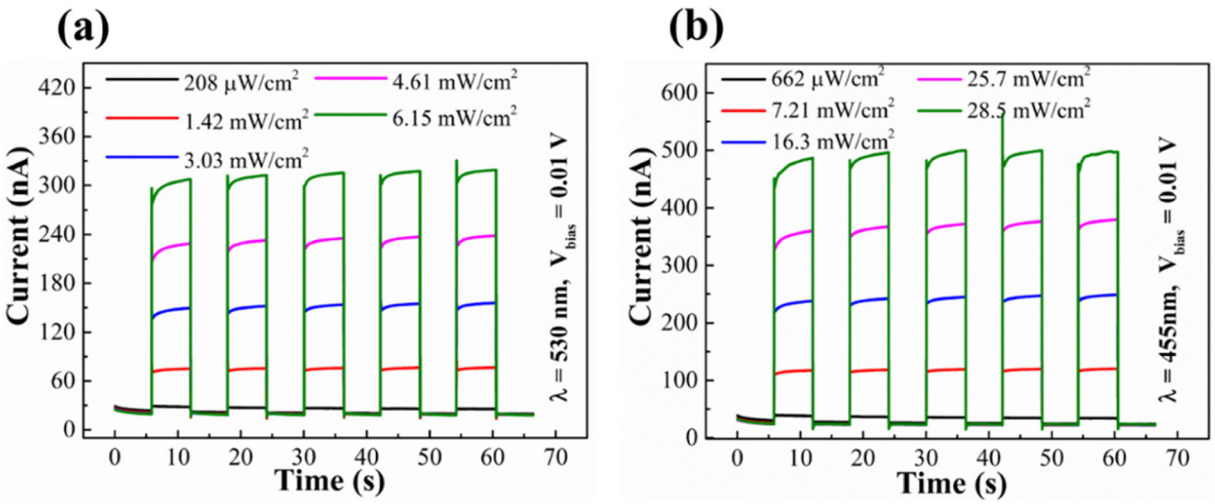


**Fig. 8** (a) Time-dependent photocurrent with different intensities at a low bias voltage (0.01 V) under (a) 530 nm and (b) 455 nm monochromatic light.

optical intensities is appreciable. It is also worth mentioning that the entire synthesis, fabrication and measurement procedures were carried out under humid weather conditions ranging from 50%–80%RH. This also depicts the robustness of the synthesized $FAPBBr_3$ NCs as well as the heterojunction device. The best values of the on-to-off ratio, $R$ and $D^*$ for our device configuration were respectively determined to be $1.44 \times 10^4$, 0.668 A $W^{-1}$and $7.78 \times 10^{11}$ Jones at 1 V bias voltage under an optical intensity of 48.27 mW $cm^{-2}$ for a 20 s on/off time interval. The corresponding $I$–$t$ curve is depicted in Fig. 9. A comparative analysis of our $ZnO/FAPbBr_3$ photodetector metrics with other reported $FAPbBr_3$ and ZnO/perovskite systems is listed in Table 2.

In comparison with previously reported $FAPbBr_3$-based photodetectors, our device demonstrates rapid switching behavior, characterized by short rise and fall times, while sustaining competitive levels of responsivity and detectivity over a wide spectral detection range. A key feature of our solution-processed architecture is the incorporation of a novel n–n type-II heterojunction between ZnO and $FAPbBr_3$. Most of the ZnO/perovskite systems reported in the literature consist of a p–n type-II heterojunction, as listed under Table 2. The choice of an appropriate photoactive layer and an appropriate architectural design strategy determines the photodetector's operating range for a dedicated application, as well as the final performance metrics.

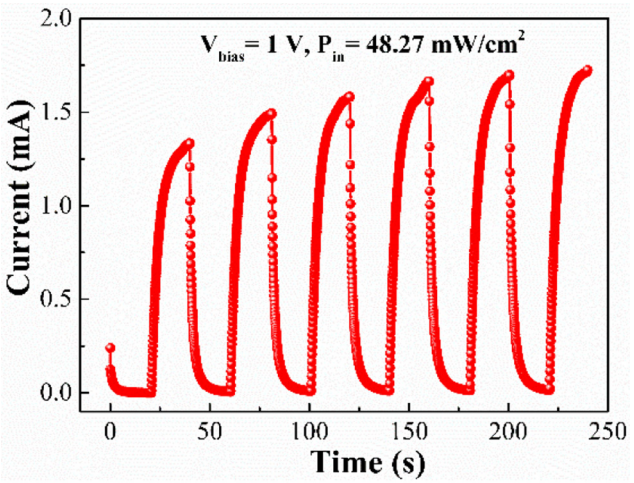


**Fig. 9** $I$–$t$ curve depicting the photoresponse behavior of the device at a reverse bias voltage of for a 20 s on-off interval.

To evaluate the individual performance of $FAPbBr_3$ NCs and ZnO, two additional device configurations were studied, FTO/$FAPbBr_3$/Ag ($D_1$) and FTO/ZnO/Ag ($D_2$). The logarithmic current–voltage (ln $I$–$V$) characteristics presented in Fig. 10a ($D_1$) and Fig. 10b ($D_2$) reveal the ohmic behavior for $D_1$ and Schottky-type behavior for $D_2$. Nevertheless, both configurations exhibit significantly higher leakage currents relative to the $ZnO/FAPbBr_3$ heterojunction device. Additionally, when subjected to white light illumination, only $D_2$ exhibits a low photoresponse, as illustrated in Fig. 10c. The $I$–$t$ profile for $D_2$, recorded at 0.5 V bias under 50 mW $cm^{-2}$, displays a diminishing pattern of photocurrent after each cycle, indicative of unstable and degrading overall device performance. However, as illustrated above, a synergy of the $ZnO/FAPbBr_3$ heterojunction produces pronounced photodetection, subject to improved absorption characteristics, appropriate band alignment, and better transport properties at the junction.

For a better understanding of the operational mechanism of the FTO/ZnO/$FAPbBr_3$/Ag photodetector, we refer to Fig. 11 (a–c). Here, both ZnO and $FAPbBr_3$ are n-type semiconductors, with ZnO serving mainly as an electron extraction layer and $FAPbBr_3$ functioning as the photosensitive absorber. The difference in the conduction band and valence band energy levels of ZnO and $FAPbBr_3$ leads to the formation of a type-II

**Table 2** Comparison of different parameters for $FAPbBr_3$-based photodetectors and other ZnO-perovskite photodetectors

| Material | Device architecture | Responsivity (mA $W^{-1}$) | Detectivity (Jones) | Rise/fall time | On/off ratio | Applied bias | Detection wavelength (nm) | Ref. |
|---|---|---|---|---|---|---|---|---|
| $FAPbBr_3$ | Au/$FAPbBr_3$/Au (lateral) | $1.03 \times 10^6$ | $1.2 \times 10^{13}$ | 25 ms | $10^4$ | 3 | 545 | 61 |
| $FAPbBr_3/NiO_x$ | Ag/$FAPbBr_3$/$NiO_x$/ITO (vertical) | $1.23 \times 10^2$ | $7.1 \times 10^{11}$ | 10 ms/200 ms | $1.8 \times 10^3$ | 0 | 450 | 36 |
| $FAPbBr_3$/Ge | Au/$FAPbBr_3$/Ge/Au SPD | $3.3 \times 10^2$ | $3.83 \times 10^{11}$ | 12.3 ms/4.9 ms | — | 0 | 520 (laser) | 35 |
| $FAPbBr_3$/C60 | Al/PCBM/$FAPbBr_3$:C60/CuPC/FTO | $1.47 \times 10^3$ | $6.39 \times 10^{10}$ | — | — | 2 | Solar irradiation | 62 |
| $FAPbBr_3$–graphene hybrid | Ag/$FAPbBr_3$–graphene/$SiO_2$/Si (vertical) | $1.15 \times 10^8$ | — | 58 ms/60 ms | — | 2 | 520 | 30 |
| $MAPbI_3$/ZnO | $MAPbI_3$/Au/ZnO/glass | $2.73 \times 10^3$ | $1.09 \times 10^{12}$ | — | $5.88 \times 10^3$ | 7 | 360 | 43 |
| $MAPbBr_3$/ZnO | Carbon/$MAPbBr_3$/ZnO/carbon/glass | 4.79 | $5.25 \times 10^{10}$ | 17.12 ms/26.27 ms | $6.1 \times 10^{23}$ | 0 | 530 | 52 |
| $Cs_2SnI_6$/ZnO | Al/$Cs_2SnI_6$/ZnO/ITO | $1.83 \times 10^2$ | $1.39 \times 10^{12}$ | 4.3 μs/5.2 μs | — | 5 | 378 | 42 |
| $CsPbBr_3$/hollow ZnO hemispherical array (ZHA) | Carbon/$CsPbBr_3$/ZHA/FTO | $10^2$ | $4.2 \times 10^{12}$ | 13 μs/28 μs | $1.04 \times 10^{63}$ | 0 | 473 | 44 |
| $CsPbBr_3$/ZnO | Ag/$CsPbBr_3$/ZnO/ITO | 79.5 | $3.96 \times 10^{11}$ | 354 ms/107 ms | $10^3$ | 1 | 450 | 45 |
| $Cs_3Bi_2I_9$/ZnO | Au/$Cs_3Bi_2I_9$/ZnO/FTO | 33.2 | $1.07 \times 10^{10}$ | 16.4 ms/16.8 ms | — | 0 | 380 | 46 |
| $Cs_3Cu_2I_5$/ZnO | Au/$Cs_3Cu_2I_5$/ZnO/Au | $3.14 \times 10^2$ | $1.26 \times 10^{11}$ | 0.43 ms/0.46 ms | 150 | 4 | 280 | 48 |
| $Cs_2AgBiBr_6/SnO_2$/ZnO | Ag/$Cs_2AgBiBr_6/SnO_2$/ZnO/FTO | $6.08 \times 10^2$ | $2.97 \times 10^{10}$ | 124 ms/61 ms | $\sim 10^2$ | 0.01 | 405 | 49 |
| $CsCu_2I_3$/ZnO | Au/$CsCu2I_3$/ZnO/ITO | $1.62 \times 10^3$ | $4.13 \times 10^{11}$ | — | — | — | 405 | 50 |
| $CsPbBr_3$/ZnO | Au/$CsPbBr_3$/ZnO/Si | $3.58 \times 10^5$ | — | 0.83 ms/1.53 ms | $10^4$ | 9 | 442 | 47 |
| $CsPbI_3$/ZnO | Al/$CsPbI_3$/ZnO/ITO | $8.2 \times 10^3$ | $1.4 \times 10^{12}$ | 25 ms/30.6 ms | $2.4 \times 10^4$ | 4 | 690 | 51 |
| 1%Er:ZnO–$CsSnCl_3$ nanowires/Si | Ti/Au/$CsSnCl_3$/Er:ZnO nanowires/Si/Al | $1.9 \times 10^2$ | $2.48 \times 10^{11}$ | 83 ms/63 ms | 339 | 0 | 378 | 41 |
| **$FAPbBr_3$/ZnO** | **Ag/$FAPbBr_3$/ZnO/FTO** | $\mathbf{6.68 \times 10^2}$ | $\mathbf{7.78 \times 10^{11}}$ | **0.08 ms/0.09 ms** | $\mathbf{1.44 \times 10^4}$ | **1** | **Solar irradiation** | **This work** |

n–n heterojunction at the ZnO/$FAPbBr_3$ interface. A type-II heterojunction provides a staircase arrangement for efficient charge separation and extraction, a configuration widely employed in optoelectronic devices such as solar cells and photodetectors. Now, as portrayed in Fig. 11, under dark conditions with no external bias, the electrons from a higher CBM of $FAPbBr_3$ flow to a lower CBM of ZnO until the Fermi levels align and an equilibrium is reached. This process creates accumulation and depletion regions at the ZnO/$FAPbBr_3$ interface, generating a built-in electric field directed towards ZnO that opposes further carrier flow (Fig. 11a). Upon applying a reverse bias (positive polarity at FTO), electrons are driven toward the anode and repelled from the cathode, thereby expanding the depletion region as shown in Fig. 11b. Furthermore, as we illuminate the junction, electron–hole pairs are generated at both the depletion region and within the photosensitive layer. The combined influence of the built-in electric field and the type-II band alignment facilitates directional carrier separation and transport, culminating in a measurable photoresponse (Fig. 11c).

II. **The memristor behavior of FTO/ZnO/$FAPbBr_3$/Ag:**

The architectural design of a device dictates its applicability across various functions, depending upon the underlying operational criteria of each application. A compelling illustration of this principle is observed in the shared structural paradigm of p–i–n photodiodes and conventional inverted perovskite solar cells, despite their separate working principles. While photodiodes operate under reverse or zero-bias conditions for the detection of broadband or narrowband optical signals, perovskite solar cells are optimized for energy generation under forward bias. Consequently, a single device architecture can exhibit multifunctional utility, depending on the physical phenomena it exploits. Targeting a memristor functionality for our device, we applied bias to the top electrode (Ag) of our ZnO/$FAPbBr_3$ heterojunction device while conducting a voltage sweep in the direction $-V_1 \rightarrow 0 \rightarrow +V_2 \rightarrow 0 \rightarrow -V_1$. As depicted in Fig. 12a, the ln $I$–$V$ plot of the device is accompanied by hysteresis when the voltage loop is repeated for 100 cycles, featuring bidirectional non-volatile memory.[63] Furthermore, from Fig. 12b, the conductance of the device increases after each positive voltage sweep from 0 V → +1.25 V → 0 V, while for a negative sweep in the direction 0 V → −1.5 V → 0 V, the conductance decreases as shown in Fig. 12c. This indicates a gradual change in the resistance of the device, which is a characteristic analog switching behavior, indifferent to an abrupt or digital switching. Such an analog resistive switching phenomenon has been widely studied amongst various active materials such as metal oxides, polymers, 2D materials, and metal halide perovskites, and across different geometries.[64–66] The change in the conductance of the system forms the basis for neuromorphic computing applications, where biological synaptic operations of the human brain are emulated. The "set" and "reset" operations, which gradually increase or decrease the conductance, directly map to long-term potentiation (LTP) and long-term depression (LTD), respectively – fundamental mechanisms for learning and memory in biologi-

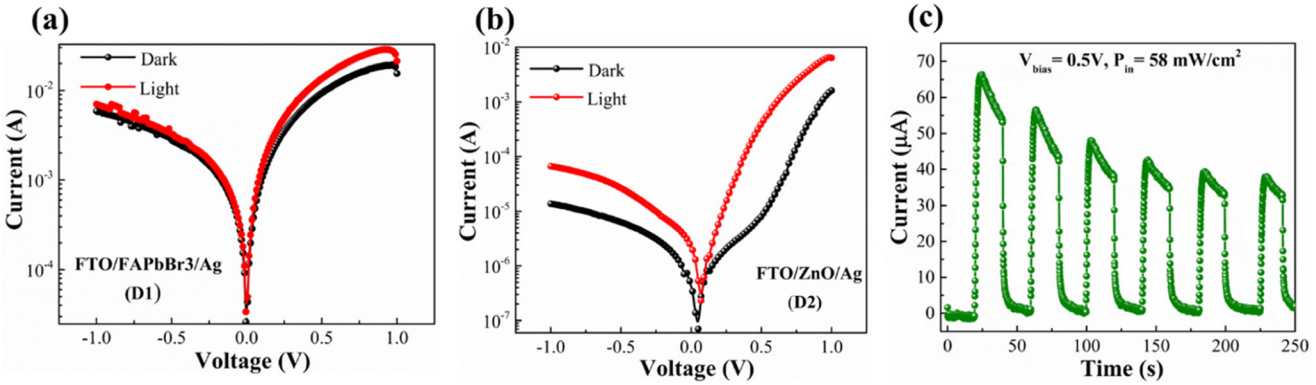


**Fig. 10** (a) Semi-logarithmic *I*–*V* characteristics for FTO/FAPbBr$_3$/Ag ($D_1$) and (b) FTO/ZnO/Ag ($D_2$). (c) *I*–*t* curve depicting the photoresponse behavior of FTO/ZnO/Ag ($D_2$) under 58 mW/cm$^{-2}$ at 0.5 V bias voltage.

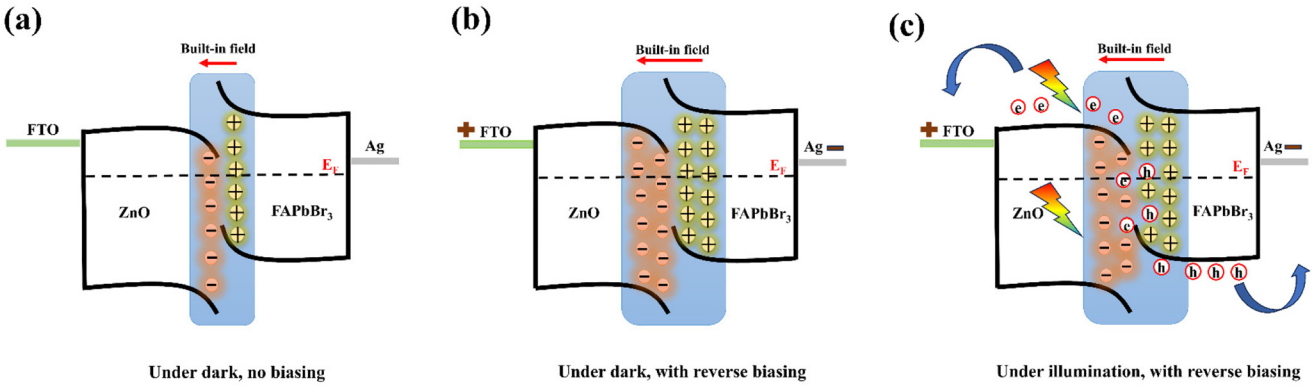


photoresponse Fig. 11c.

**Fig. 11** Schematics representing the working mechanism of under (a) darkness with no applied biasing, (b) darkness with an applied reverse bias, and (c) illumination with a reverse bias.

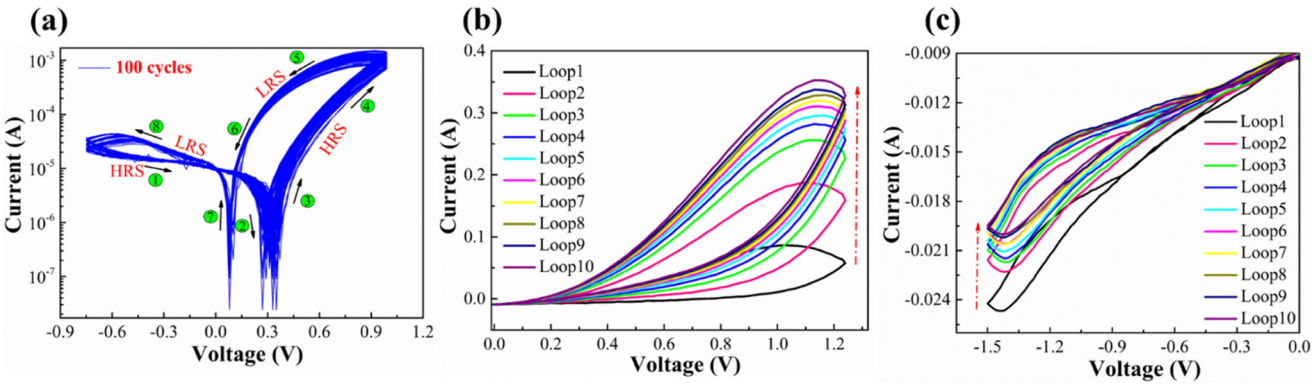


**Fig. 12** *I*–*V* characteristics of the FTO/ZnO/FAPbBr$_3$/Ag device showing (a) bipolar analog resistive switching behaviour for 100 voltage sweep cycles, (b) 10 consecutive loops in the positive voltage sweep direction 0 V → 1.25 V → 0 V, (c) 10 consecutive loops in the negative voltage sweep direction 0 V → –1.5 V → 0 V.

cal brains. The proposed device under study, FTO/ZnO/FAPbBr$_3$/Ag, therefore, can show a dual functionality when suitably biased.

Furthermore, to confirm the underlying switching mechanism of our device, the *I*–*V* curve was replotted in the double-logarithmic scale for both positive and negative voltage

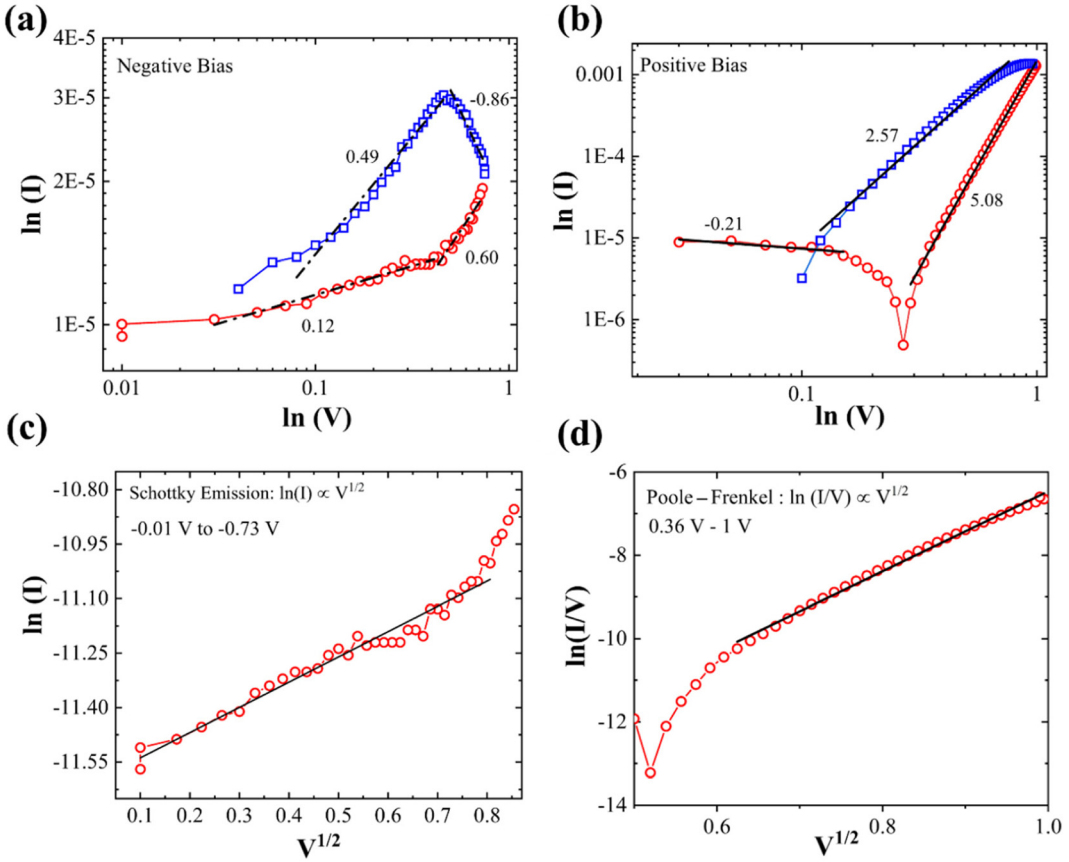


**Fig. 13** Conduction mechanism based on Child's law, represented using ln(*I*) *vs.* ln(*V*) (a) for positive bias, (b) for negative bias, (c) Schottky emission from ln(*I*) *vs.* $V^{1/2}$ for the negative bias region of HRS, (d) Poole–Frenkel mechanism from ln(*I*/*V*) *vs.* $V^{1/2}$ from the positive voltage region of HRS.

regions. The fitted slope values of the respective curves indicate the existing conduction mechanisms, such as ohmic conduction ($I \propto V$), space charge limited conduction (SCLC) ($I \propto V^2$), Schottky emission ($I \propto V^{1/2}$), Poole–Frenkel conduction (ln ($I/V$) $\propto V^{1/2}$), or trap-assisted tunnelling (ln($I/V$) $\propto V$).[67–69] Fig. 13a and b present the ln *I vs.* ln *V* plot for negative and positive voltage ranges, respectively. The HRS is indicated by red circles, while the blue circles represent the LRS of the device across various bias regions. The HRS in the negative voltage region and low-bias positive voltage region depicts non-linear slope values of 0.21, 0.6 and −0.21, as illustrated in Fig. 13a and b. A fitted slope value of 5.08, indicative of an SCLC mechanism, is evident in the higher positive voltage region. To realise the actual conduction mechanism of the HRS in the negative bias region (−0.01 V to −0.73 V), we further fitted the data with an ln($I$) *vs.* $V^{1/2}$ curve, as shown in Fig. 13c. The linearity of this curve indicates a Schottky emission mechanism in this bias range. Similarly, a linear dependence of the ln($I/V$) *vs.* $V^{1/2}$ curve (Fig. 13d) in the positive bias region (0.36 V to 1 V) indicates a Poole–Frenkel conduction mechanism. For the negative voltage region of the LRS (Fig. 13a), a slope value of 0.49, indicating a Schottky conduction mechanism, and a negative slope value of 0.86 for ionic conduction, are evident in the lower and higher bias ranges, respectively. Meanwhile, the positive voltage region of LRS (Fig. 13b) predominantly indicated an SCLC mechanism with an ln *I vs.* ln *V* slope of 2.57. Based on the above analysis of the gradual switching behaviour of our device, we predict that interfacial state modulation and ionic migration can form the basis of resistive switching, rather than metallic filamentary conduction.[68,70] Fig. 14a–c show the possible conduction mechanism for FTO/ZnO/$FAPbBr_3$/Ag, based on the halide ion migration and vacancy defects.[71,72]

Due to the low defect formation energy of halide ions in perovskites,[73] the $FAPbBr_3$ framework consists of dispersed negatively charged bromine ions ($Br^-$) and their respective bromine vacancies ($V_{Br}$) in the initial state with no applied field (Fig. 14a). As we provide a positive potential to the Ag electrode, the $Br^-$ ions drift towards the top electrode, leaving behind the bromine vacancies ($V_{Br}$) in the bulk of the perovskite. These vacancies ($V_{Br}$) form a conductive ionic path in the direction of the electric field towards the FTO, through which the injected electrons can travel, thereby triggering the SET process or low resistance state of the device.[68] Additionally, some Ag atoms may ionise to $Ag^+$ ions and drift towards the bulk of the perovskite, but this remains insufficient for metallic filament formation in the device. Now, on reversing the polarity of the applied potential, as shown in Fig. 14c, the $Br^-$

 

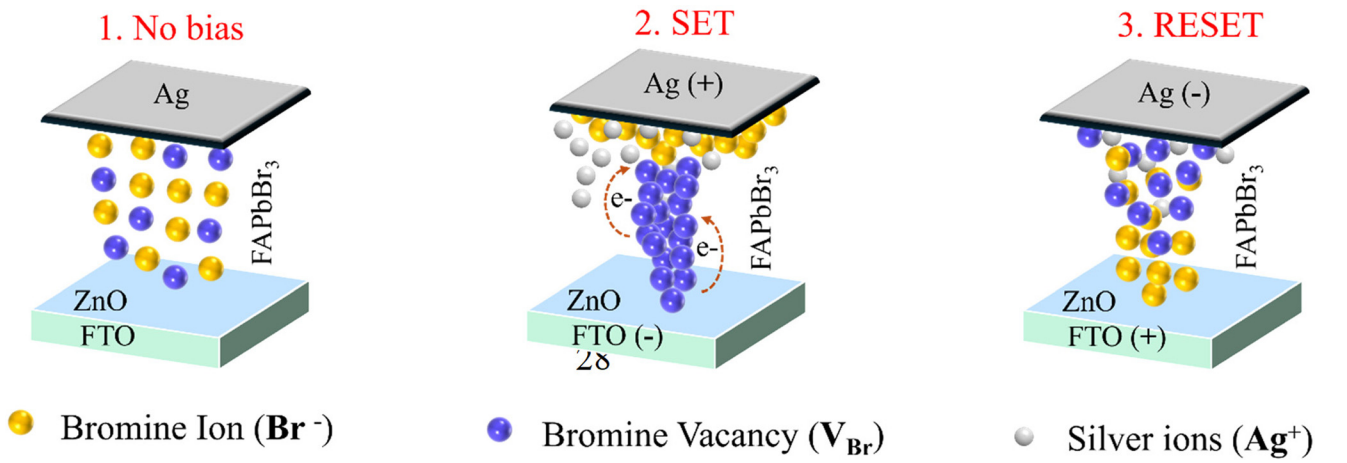


**Fig. 14** Schematic representation of the switching mechanism, depicting (1) the initial state with no external biasing, (2) the SET condition, and (3) the RESET condition.



ions will move away from the Ag electrode and, in this process, will dissolve some of the vacancy sites, thereby disrupting the conduction channel. This process resets the device and marks the transition from the LRS to the HRS. With the application of a large negative bias, rectifying behaviour is manifested due to the Schottky barrier formation at the $FAPbBr_3$/Ag interface, which hinders the electron flow and limits the current magnitude to the HRS.

## 5. Conclusion

To summarize, we developed an n–n heterojunction photodetector based on ZnO/$FAPbBr_3$ NCs using easy solution processing methods. Our device achieves a high on-to-off ratio of approximately $1.44 \times 10^4$, a good responsivity of 0.668 A $W^{-1}$, and a specific detectivity of $7.78 \times 10^{11}$ Jones at an operating voltage of 1 V under 48.27 mW $cm^{-2}$ white-light illumination. Analysis of the optoelectronic behavior at various low operating voltages (0 to 0.9 V) and different white-light intensities (40.19 to 137.32 mW $cm^{-2}$) shows that the device performs optimally under low to moderate white light levels with appropriate biasing. The detector also exhibits fast switching times of 80 μs/90 μs at a transient frequency of 3 kHz. Overall, the fast response and good sensitivity of the detector are attractive for imaging technologies, ranging from biomedical diagnostics to environmental monitoring. Apart from this, the device depicts a bidirectional resistive switching phenomenon when operated under a cyclic voltage loop. The gradual change in the conductance of the system symbolizes an analog behavior that can effectively mimic neural operations of learning and forgetting in the human brain. While initial switching responses of the device to voltage sweeps are presented, a comprehensive investigation of its neuromorphic capabilities remains beyond the scope of this study. Overall, this work highlights the multifunctionality of the novel ZnO/$FAPbBr_3$ n–n heterojunction device, serving both as a low-bias, fast, broadband photodetector and as an analog memristor with promising potential for future neuromorphic applications.

## Author contributions

Monisha Nayak: material synthesis, device fabrication, investigation, data acquisition, formal analysis, writing—original draft, conceptualization, and funding acquisition. Ashutosh Mohanty: material characterization (XRD, HR-TEM, XPS), data acquisition for transient and LED measurements, and scientific discussion. Pragalbh Kashyap: SEM analysis. Abhijit Bar: designing the software for photodetection measurements and IPCE measurement. Sudip K. Saha: funding acquisition, resources, scientific discussion, draft reviewing, editing, and finalizing.

## Conflicts of interest

The authors declare no conflict of interest.

## Data availability

The datasets generated during and/or analysed during the current study are available from the corresponding author on reasonable request.

Supplementary information (SI) is available. See DOI: https://doi.org/10.1039/d5nr04337a.

## Acknowledgements

MN acknowledges DST Inspire Fellowship Code IF190229 for financial support. SKS acknowledges the financial support from UGC-DAE CSR through a Collaborative Research Scheme (CRS) CRS/2022-23/04/896. The authors gratefully

acknowledge UGC-DAE Consortium for Scientific Research, Kolkata Centre, and Dr Gautam Pramanik for facilitating time-correlated single photon counting (TCSPC) measurements. The authors are also thankful to the North East Centre for Biological Sciences and Healthcare Engineering (NECBH), IIT Guwahati, for performing FE-SEM measurements of the samples.

## References

1 P. C. Y. Chow and T. Someya, Organic Photodetectors for Next-Generation Wearable Electronics, *Adv. Mater.*, 2020, **32**(15), 1902045.
2 X. Feng, C. Li, J. Song, Y. He, W. Qu, W. Li, *et al.*, Differential perovskite hemispherical photodetector for intelligent imaging and location tracking, *Nat. Commun.*, 2024, **15**(1), 577.
3 H. Ren, J.-D. Chen, Y.-Q. Li and J.-X. Tang, Recent Progress in Organic Photodetectors and their Applications, *Adv. Sci.*, 2021, **8**(1), 2002418.
4 S. Rezaei-Mazinani, A. I. Ivanov, C. M. Proctor, P. Gkoupidenis, C. Bernard, G. G. Malliaras, *et al.*, Monitoring Intrinsic Optical Signals in Brain Tissue with Organic Photodetectors, *Adv. Mater. Technol.*, 2018, **3**(5), 1700333.
5 Z. Wang, Y. Gao, Y. Li, H. Yan, F. Kang, Y. Shen, *et al.*, High Speed Dual-Band Photodetector for Dual-Channel Optical Communications in Wavelength Division Multiplexing and Security Enhancement, *Adv. Funct. Mater.*, 2024, **34**(17), 2310911.
6 C. Buchal, M. Löken, T. Lipinsky, L. Kappius and S. Mantl, Ultrafast silicon based photodetectors, *J. Vac. Sci. Technol., A*, 2000, **18**(2), 630–634.
7 D.-M. Geum, J. Lim, J. Jang, S. Ahn, S. Kim, J. Shim, *et al.*, Highly-efficient (>70%) and Wide-spectral (400–1700 nm) sub-micron-thick InGaAs photodiodes for future high-resolution image sensors, *Light: Sci. Appl.*, 2024, **13**(1), 311.
8 H. D. Jabbar, M. A. Fakhri and M. Jalal AbdulRazzaq, Gallium Nitride –Based Photodiode: A review, *Mater. Today: Proc.*, 2021, **42**, 2829–2834.
9 X. Qiu, X. Yu, S. Yuan, Y. Gao, X. Liu, Y. Xu, *et al.*, Trap Assisted Bulk Silicon Photodetector with High Photoconductive Gain, Low Noise, and Fast Response by Ag Hyperdoping, *Adv. Opt. Mater.*, 2018, **6**(3), 1700638.
10 R. Velazquez, A. Aldalbahi, M. Rivera and P. Feng, Fabrications and application of single crystalline GaN for high-performance deep UV photodetectors, *AIP Adv.*, 2016, **6**(8), 085117.
11 N. K. R. Nallabala, V. R. M. Reddy, V. R. Singh, K. R. Bakash, S. Kumar, D. Saha, *et al.*, Enhanced photoresponse performance in GaN based symmetric type MSM ultraviolet-A and MIS ultraviolet-A to C photodetectors, *Sens. Actuators, A*, 2022, **339**, 113502.
12 N. K. R. Nallabala, S. S. Kushvaha, S. Sangaraju and V. K. Kummara, Enhanced self-driven ultraviolet photodetection performance of high-k Ta2O5/GaN heterostructure, *Mater. Sci. Semicond. Process.*, 2024, **170**, 107954.
13 N. K. R. Nallabala, S. Godavarthi, V. K. Kummara, M. K. Kesarla, C. Yuvaraj, K. Suresh, *et al.*, High performance, self-powered and thermally stable 200–750 nm spectral responsive gallium nitride (GaN) based broadband photodetectors, *Sol. Energy Mater. Sol. Cells*, 2021, **225**, 111033.
14 N. K. R. Nallabala, S. V. P. Vattikuti, V. K. Verma, V. R. Singh, S. Alhammadi, V. K. Kummara, *et al.*, Highly sensitive and cost-effective metal-semiconductor-metal asymmetric type Schottky metallization based ultraviolet photodetecting sensors fabricated on n-type GaN, *Mater. Sci. Semicond. Process.*, 2022, **138**, 106297.
15 N. Huo and G. Konstantatos, Recent Progress and Future Prospects of 2D-Based Photodetectors, *Adv. Mater.*, 2018, **30**(51), 1801164.
16 J. S. Manser, J. A. Christians and P. V. Kamat, Intriguing Optoelectronic Properties of Metal Halide Perovskites, *Chem. Rev.*, 2016, **116**(21), 12956–13008.
17 A. Dey, J. Ye, A. De, E. Debroye, S. K. Ha, E. Bladt, *et al.*, State of the Art and Prospects for Halide Perovskite Nanocrystals, *ACS Nano*, 2021, **15**(7), 10775–10981.
18 M. T. Hoang, F. Ünlü, W. Martens, J. Bell, S. Mathur and H. Wang, Towards the environmentally friendly solution processing of metal halide perovskite technology, *Green Chem.*, 2021, **23**(15), 5302–5336.
19 L. Dou, Y. Yang, J. You, Z. Hong, W.-H. Chang, G. Li, *et al.*, Solution-processed hybrid perovskite photodetectors with high detectivity, *Nat. Commun.*, 2014, **5**(1), 5404.
20 M. Nayak, A. J. Akthar, A. Guchhait and S. K. Saha, A roadmap towards stable perovskite solar cells: prospective on substitution of organic (A) & inorganic (B) cations, *J. Mater. Sci.: Mater. Electron.*, 2021, **32**(14), 18466–18511.
21 Y. Li, F. Z. Liu, M. Waqas, T. L. Leung, H. W. Tam, X. Q. Lan, *et al.*, Formamidinium-Based Lead Halide Perovskites: Structure, Properties, and Fabrication Methodologies, *Small Methods*, 2018, **2**(7), 1700387.
22 M. Nayak, A. J. Akhtar and S. K. Saha, Theoretical estimation to double the performance of perovskite solar cells using a graded absorber layer, *Sustainable Energy Fuels*, 2025, **9**(5), 1305–1316.
23 P. K. Singha, A. Kumar, A. Gupta and A. Datta, Formamidinium Lead Bromide Nanocrystals Doped with In3 + and Cl– for Light-Emitting Applications, *ACS Appl. Nano Mater.*, 2025, **8**(18), 9110–9119.
24 H. Zhang, S. Zhang, X. Ji, J. He, H. Guo, S. Wang, *et al.*, Formamidinium Lead Iodide-Based Inverted Perovskite Solar Cells with Efficiency over 25 % Enabled by An Amphiphilic Molecular Hole-Transporter, *Angew. Chem., Int. Ed.*, 2024, **63**(16), e202401260.
25 M. Nayak, R. Nag, A. Bera, A. J. Akhtar and S. K. Saha, Schottky analysis of formamidinium lead halide perovskite nanocrystals' devices with enhanced stability, *Appl. Nanosci.*, 2022, **12**(9), 2671–2681.
26 M. Nayak, R. Nag, A. Bera, P. Samanta, A. J. Akhtar and S. K. Saha, *In situ* fabricated poly (vinylidene fluoride)-

 

Incorporated perovskite nanocrystals with better Schottky performance and enhanced stability, *Opt. Mater.*, 2023, **138**, 113685.

27 M. Nayak, A. J. Akhtar and S. K. Saha, Low-cost, stable all-inorganic charge transporting layer based FAPI perovskite solar cells achieving ≈ 26% efficiency using SCAPS-1D, *Optik*, 2024, **303**, 171727.

28 R. Gupta, V. Gupta, R. Datt, S. Arya, A. Pandey, A. Singh, *et al.*, Enhanced photosensitive properties of a single-crystal formamidinium lead bromide iodine (FAPbBr2I) based photodetector, *Mater. Adv.*, 2022, **3**(4), 2089–2095.

29 M. Zhang, F. Zhang, Y. Wang, L. Zhu, Y. Hu, Z. Lou, *et al.*, High-Performance Photodiode-Type Photodetectors Based on Polycrystalline Formamidinium Lead Iodide Perovskite Thin Films, *Sci. Rep.*, 2018, **8**(1), 11157.

30 R. Pan, H. Li, J. Wang, X. Jin, Q. Li, Z. Wu, *et al.*, High-Responsivity Photodetectors Based on Formamidinium Lead Halide Perovskite Quantum Dot–Graphene Hybrid, *Part. Part. Syst. Charact.*, 2018, **35**(4), 1700304.

31 D. Sahu, S. Debnath, S. Ghosal and P. K. Giri, 2D Printed Plasmonic Nanoparticle Array Incorporated Formamidinium-Based High-Performance Self-Biased Perovskite Photodetector, *ACS Appl. Mater. Interfaces*, 2024, **16**(37), 49544–49555.

32 G. Chen, Y. Qiu, H. Gao, Y. Zhao, J. Feng, L. Jiang, *et al.*, Air-Stable Highly Crystalline Formamidinium Perovskite 1D Structures for Ultrasensitive Photodetectors, *Adv. Funct. Mater.*, 2020, **30**(14), 1908894.

33 Y. Xiong, B. Chen, R. Zhang, J. Zhang, Y. Zhan and X. Xu, Synergy of Micro-Nano Engineering Templates and Additives for FAPbI3-Based 1D Triangular Array Photodetector Fabrication, *Adv. Funct. Mater.*, 2025, 2501403.

34 J.-H. Shen, X.-Q. Yu and W.-C. Tu, Multifunctional and High-Performance FAPBI3 Quantum Dots/Graphene UV Photodetectors by the Modulation of Photoconductivity, *Adv. Opt. Mater.*, 2023, **11**(17), 2300410.

35 Z. Wang, X. Geng, J. Jin, P. Zhang, L. Zhang, Y. Li, *et al.*, Self-Powered Photodetector Based on Perovskite/Ge Heterojunction with High Responsivity, *Adv. Mater. Technol.*, 2024, **9**(8), 2301819.

36 K. Tao, C. Xiong, J. Lin, D. Ma, S. Lin, B. Wang, *et al.*, Self-Powered Photodetector Based on Perovskite/NiOx Heterostructure for Sensitive Visible Light and X-Ray Detection, *Adv. Electron. Mater.*, 2023, **9**(3), 2201222.

37 S. Bansal, K. Prakash, K. Sharma, N. Sardana, S. Kumar, N. Gupta, *et al.*, A highly efficient bilayer graphene/ZnO/silicon nanowire based heterojunction photodetector with broadband spectral response, *Nanotechnology*, 2020, **31**(40), 405205.

38 S. Bansal, A. K. Rajpoot, G. Chamundeswari, K. Prakash, P. R. Kumar, A. N. Z. Rashed, *et al.*, Pt/ZnO and Pt/few-layer graphene/ZnO Schottky devices with Al ohmic contacts using Atlas simulation and machine learning, *J. Sci.: Adv. Mater. Devices*, 2024, **9**(4), 100798.

39 S. Bansal, S. Kumar, A. Jain, V. Rohilla, K. Prakash, A. Gupta, *et al.*, Design and TCAD analysis of few-layer graphene/ZnO nanowires heterojunction-based photodetector in UV spectral region, *Sci. Rep.*, 2025, **15**(1), 7762.

40 S. Bansal, A. Bansal, K. Prakash, P. Patial, K. Kaur, A. Gupta, *et al.*, Analysis of Few-Layer Graphene/ZnO Nanowires Photodetector on Si Substrate for 6G and IoT Applications, *J. Electron. Mater.*, 2025, **54**(10), 9099–9111.

41 A. Kumar, R. Saha, A. Dalal, A. Mondal and S. Chakrabarti, Investigation of highly efficient self-powered photo-detector performance of all inorganic lead-free halide perovskites (CsSnCl3) nanocrystals (NCs) decorated Er: ZnO nanowires (NWs)/Si heterojunctions, *Opt. Mater.*, 2024, **147**, 114671.

42 D. Shao, W. Zhu, G. Xin, X. Liu, T. Wang, S. Shi, *et al.*, A high performance UV–visible dual-band photodetector based on an inorganic Cs2SnI6 perovskite/ZnO heterojunction structure, *J. Mater. Chem. C*, 2020, **8**(5), 1819–1825.

43 Y. Peng, D. Jiang, M. Zhao, Y. Duan, H. Wei, H. Li, *et al.*, High-performance UV–visible photodetectors based on ZnO/perovskite heterostructures, *J. Alloys Compd.*, 2023, **965**, 171372.

44 X. Pan, J. Zhang, H. Zhou, R. Liu, D. Wu, R. Wang, *et al.*, Single-Layer ZnO Hollow Hemispheres Enable High-Performance Self-Powered Perovskite Photodetector for Optical Communication, *Nano-Micro Lett.*, 2021, **13**(1), 70.

45 S. Wang, S. Yang, Z. Xu, H. Xu, G. Duan, D. Zhao, *et al.*, A high-performance photodetector based on a ZnO/$CsPbBr_3$ quantum-dot-level-contact hybrid sandwich structure, *J. Mater. Chem. C*, 2025, **13**(2), 902–909.

46 W. Ouyang, Self-Powered Cs3Bi2I9/ZnO Heterojunction Photodetector with Dual-Band Photoresponse, *Adv. Electron. Mater.*, 2025, **11**(3), 2400514.

47 Y. Shen, C. Wei, L. Ma, S. Wang, X. Wang, X. Xu, *et al.*, In situ formation of $CsPbBr_3$/ZnO bulk heterojunctions towards photodetectors with ultrahigh responsivity, *J. Mater. Chem. C*, 2018, **6**(45), 12164–12169.

48 X. Zhao, Y. Tao, J. Dong, Y. Fang, X. Song and Z. Yan, Cs3Cu2I5/ZnO Heterostructure for Flexible Visible-Blind Ultraviolet Photodetection, *ACS Appl. Mater. Interfaces*, 2022, **14**(38), 43490–43497.

49 W. Shen, U. Jung, Z. Xian, B. Jung and J. Park, Enhanced device performance of Cs2AgBiBr6 double perovskite photodetector by SnO2/ZnO double electron transport layer, *J. Alloys Compd.*, 2022, **929**, 167329.

50 X. Zhao, J. Dai, J. Dong, Y. Tao, J. Chen, X. Song, *et al.*, Lead-free perovskite/ZnO heterostructure for flexible visible-blind ultraviolet photodetection, *Appl. Phys. Lett.*, 2024, **124**, 253301.

51 S. Pal, A. Ghorai, S. Mahato and S. K. Ray, Piezo-Phototronic Effect-Induced Self-Powered Broadband Photodetectors using Environmentally Stable α-CsPbI3 Perovskite Nanocrystals, *Adv. Opt. Mater.*, 2023, **11**(16), 2300233.

52 L. Chu, C. Xu, D. Liu, C. Nie, X. Zhou and L. Deng, A high-performance self-powered broadband photodetector based

on vertical MAPbBr3/ZnO heterojunction, *Mater. Sci. Semicond. Process.*, 2024, **169**, 107943.
53 D. Liu, Y. Guo, M. Que, X. Yin, J. Liu, H. Xie, *et al.*, Metal halide perovskite nanocrystals: application in high-performance photodetectors, *Mater. Adv.*, 2021, **2**(3), 856–879.
54 H. Wang and D. H. Kim, Perovskite-based photodetectors: materials and devices, *Chem. Soc. Rev.*, 2017, **46**(17), 5204–5236.
55 W. G. Oldham and A. G. Milnes, n-n Semiconductor heterojunctions, *Solid-State Electron.*, 1963, **6**(2), 121–132.
56 Z. Zheng, X. Zu, Y. Zhang and W. Zhou, Rational design of type-II nano-heterojunctions for nanoscale optoelectronics, *Mater. Today Phys.*, 2020, **15**, 100262.
57 S. Ghimire, V. C. Nair, C. Muthu, K.-i. Yuyama, M. Vacha and V. Biju, Photoinduced photoluminescence enhancement in self-assembled clusters of formamidinium lead bromide perovskite nanocrystals, *Nanoscale*, 2019, **11**(19), 9335–9340.
58 H. Chen, L. Fan, R. Zhang, C. Bao, H. Zhao, W. Xiang, *et al.*, High-Efficiency Formamidinium Lead Bromide Perovskite Nanocrystal-Based Light-Emitting Diodes Fabricated via a Surface Defect Self-Passivation Strategy, *Adv. Opt. Mater.*, 2020, **8**(6), 1901390.
59 A. Perumal, S. Shendre, M. Li, Y. K. E. Tay, V. K. Sharma, S. Chen, *et al.*, High brightness formamidinium lead bromide perovskite nanocrystal light emitting devices, *Sci. Rep.*, 2016, **6**(1), 36733.
60 G. W. Mudd, S. A. Svatek, L. Hague, O. Makarovsky, Z. R. Kudrynskyi, C. J. Mellor, *et al.*, High Broad-Band Photoresponsivity of Mechanically Formed InSe–Graphene van der Waals Heterostructures, *Adv. Mater.*, 2015, **27**(25), 3760–3766.
61 X. Shi, C. Liu, X. Zhang, G. Zhan, Y. Cai, D. Zhou, *et al.*, Vapor Phase Growth of Air-Stable Hybrid Perovskite FAPbBr3 Single-Crystalline Nanosheets, *Nano Lett.*, 2024, **24**(7), 2299–2307.
62 P. Diwakar, A. Upadhyaya, S. K. Gupta and C. M. S. Negi, Self-powered solution-processed photodetectors utilizing FAPbBr3:C60 bulk heterojunction, *Opt. Mater.*, 2024, **147**, 114623.
63 W. Zhang, B. Gao, J. Tang, X. Li, W. Wu, H. Qian, *et al.*, Analog-Type Resistive Switching Devices for Neuromorphic Computing, *Phys. Status Solidi RRL*, 2019, **13**(10), 1900204.
64 S. Kunwar, Z. Jernigan, Z. Hughes, C. Somodi, M. D. Saccone, F. Caravelli, *et al.*, An Interface-Type Memristive Device for Artificial Synapse and Neuromorphic Computing, *Adv. Intell. Syst.*, 2023, **5**(8), 2300035.
65 A. Mohanty and D. Gupta, Symmetric bipolar resistive switching in copper oxide nanostructure/ITO lateral device under exposure to atmospheric oxygen and application in artificial synaptic devices, *Mater. Today Commun.*, 2023, **37**, 107546.
66 S. Satapathi, K. Raj, Yukta and M. A. Afroz, Halide-Perovskite-Based Memristor Devices and Their Application in Neuromorphic Computing, *Phys. Rev. Appl.*, 2022, **18**(1), 017001.
67 L. Tao, B. Jiang, S. Ma, Y. Zhang, Y. Huang, Y. Pan, *et al.*, 3D trigonal FAPbI3-based multilevel resistive switching nonvolatile memory for artificial neural synapse, *SmartMat*, 2024, **5**(3), e1233.
68 Y.-S. Chen, C. C. Lin, C. W. Lin, S. Y. Tsai and F.-H. Ko, CsBr Immersion for Organic–Inorganic Hybrid Perovskite-Based Memristors: Controllable Grain, Poole–Frenkel Emission, and Electrical Properties, *ACS Appl. Electron. Mater.*, 2023, **5**(11), 5916–5927.
69 X. Cao, W. Li, Q. Zheng, J. Meng, L. Yang, L. Wang, *et al.*, High-Performance Artificial Synapse Device Based on $Cs_3Bi_2Br_9$/NiO Heterostructure for Bio-Inspired Neuromorphic Computing, *ACS Appl. Mater. Interfaces*, 2025, **17**(44), 60775–60788.
70 H. Ran, Z. Ren, J. Li, B. Sun, T. Wang, D. Gu, *et al.*, Self-Rectifying Switching Memory Based on HfOx/FeOx Semiconductor Heterostructure for Neuromorphic Computing, *Adv. Funct. Mater.*, 2025, **35**(13), 2418113.
71 M. K. Thakan, M. Khemnani, J. Gosai, A. Solanki and V. Kheraj, Investigations on Resistive Switching Mechanisms of Fluorinated Ruddlesden–Popper Perovskite-Based Memristors for Nociceptor Application, *ACS Appl. Mater. Interfaces*, 2025, **17**(41), 57343–57354.
72 S.-Y. Kim, H. Zhang and J. Rubio-Magnieto, Operating Mechanism Principles and Advancements for Halide Perovskite-Based Memristors and Neuromorphic Devices, *J. Phys. Chem. Lett.*, 2024, **15**(40), 10087–10103.
73 A. Oranskaia, J. Yin, O. M. Bakr, J.-L. Brédas and O. F. Mohammed, Halogen Migration in Hybrid Perovskites: The Organic Cation Matters, *J. Phys. Chem. Lett.*, 2018, **9**(18), 5474–5480.